Composites Part B 261 (2023) 110791

Contents lists available at ScienceDirect

Composites Part B

journal homepage: www.elsevier.com/locate/composites

A novel profiling concept leading to a significant increase in the mechanical performance of metal to composite adhesive joints

Adam D. Whitehouse [a,*], Victor Médeau [a], Lorenzo Mencattelli [a], Bamber Blackman [b], Silvestre T. Pinho [a,*]

[a] Department of Aeronautics, Imperial College London, London, South Kensington, SW7 2AZ, UK
[b] Department of Mechanical Engineering, Imperial College London, London, South Kensington, SW7 2AZ, UK

ARTICLE INFO

Dataset link: https://doi.org/10.17632/stg935v3pk.1

Keywords:
A. Polymer–matrix composites (PMCs)
B. Adhesion
B. Stress concentrations
B. Fracture

ABSTRACT

Traditional adhesive joints with straight edged adherends suffer from a significant stress concentration in the composite coincident with the edge of the metal adherend, which can lead to accelerated translaminar failure of the substrate. In this work, we developed a novel profiling concept which improves the mechanical performance of adhesive joints between metallic adherends and composite substrates. We conducted quasi-static four-point bending (4PB) tests which showed that profiling the edge of the metallic adherend could improve the peak load by at least 27%, and that the stability of failure was simultaneously improved. We investigated varying the profile parameters and were able to conclude that further significant mechanical performance gains could be achieved by increasing any of the profile: amplitude, frequency, or number of fractal length-scales. By analysing in-situ acoustic emission (AE) monitoring data we were able to observe that profiling of the metallic adherend results in failure initiation occurring at higher loads, which suggests that the concept is successful in providing better stress distributions and lowering peak stresses. By analysing the fracture surfaces, it is apparent that the profiling concept is successful in deflecting the translaminar fracture path; and additionally that a debonding mechanism occurs at the profile tips which is thought to be an important additional mechanism for creating damage tolerant joints.

1. Introduction

1.1. Stress concentration at adhesive joints

Adhesive joining of metal and composites offers many advantages over traditional mechanical joining methods such as riveting [1]. In addition to providing a high joining strength, the use of adhesives provides improved stress distributions [2] due to a continuous and relatively larger connecting area. Whilst adhesive joints do offer an improved stress distribution, a step change in stiffness at the edge of the joint means that a significant stress concentration is still present [3–5]. This can lead to the failure mechanism depicted in Fig. 1.

Fig. 1 shows that the concentration of peel stress initiates interlaminar failure. The delaminated plies subsequently suffer a translaminar fracture, which, due to the stress concentration running continuously along the joint edge, is encouraged to rapidly propagate across the joint width. This failure then allows the delaminations to propagate resulting in an unstable failure.

1.2. Industrial significance

Jet engine fan blades are often subject to bird strike events which impart high-velocity transverse impact loads. The aerospace industry has begun to utilise composite fan blades with adhesively bonded metallic erosion shields [6,7], so a stress concentration in the composite blade at the edge of the erosion shield may lead to accelerated failure of the component, and ultimately to a blade-off event which could compromise the safety of the structure. Composite helicopter rotors [8] and aeroplane wings [9] with metallic leading edge erosion shields could both similarly be vulnerable to failure triggered by this stress concentration following hail or bird strikes.

In the energy sector, leading-edge erosion is a significant problem for off-shore wind turbines. Larger turbines which give greater efficiencies, also have increased tip speeds, which has led to blades suffering significant erosion damage just a few years into their supposed 25-year service life [10]. Metallic erosion shields have been shown to offer a lifetime greater than that of the blade service life [10,11]; however,

* Corresponding authors.
E-mail addresses: adw15@ic.ac.uk (A.D. Whitehouse), silvestre.pinho@imperial.ac.uk (S.T. Pinho).
URL: https://pinholab.cc.ic.ac.uk/ (S.T. Pinho).

https://doi.org/10.1016/j.compositesb.2023.110791
Received 20 January 2023; Received in revised form 27 April 2023; Accepted 3 May 2023
Available online 9 May 2023

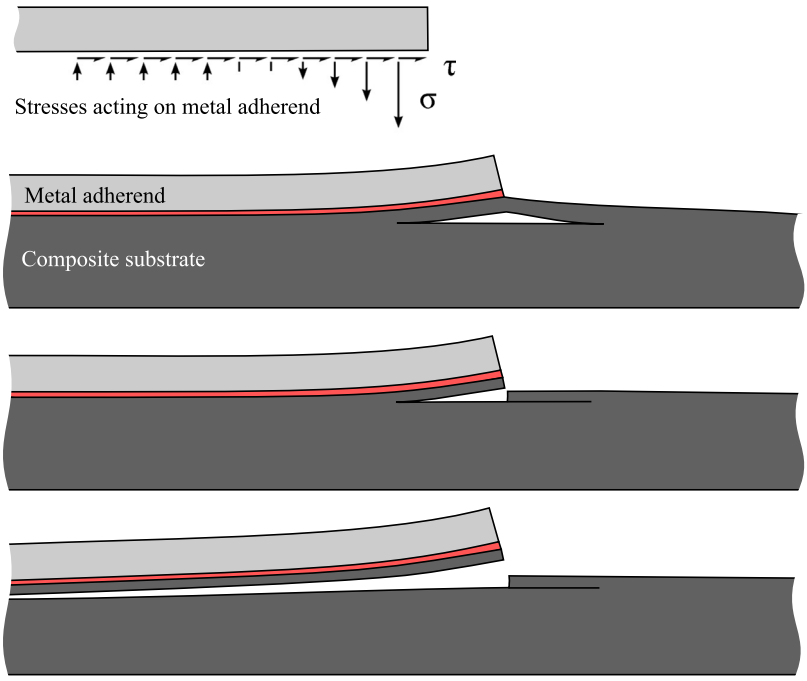

Fig. 1. The sequence of failure at the adherend edge. Recreation based on Hart-Smith et al. [4].

the stiffness mismatch of a metallic erosion shield with the composite blade is then a design concern. Herring et al. [10] have suggested that a design that can account for this stiffness mismatch may reveal the solution to leading edge erosion in off-shore wind turbines.

Beyond erosion shields, there are other applications and loading scenarios where this type of failure is of relevance. From structural applications with joints transferring axial loads, an active area of research [12], to more complexly loaded components, such as safety structures in motorsport. A recent high-profile example is the crash of Formula (1) driver Zhou Guanyu at the start of the 2022 British Grand Prix, where the solid titanium roll hoop of the car, that was adhesively bonded to the CFRP monocoque, was torn off the car with the process of failure appearing to follow the same failure mechanism [13]. If a concept can be developed which significantly improves the mechanical performance of metal to composite adhesive joints, it will have a large significance across a number of industries.

1.3. Background

There has been significant work in the literature to address the failure of structural adhesive joints, with researchers exploring solutions ranging from new joint configurations, to adding nanostructure to the adhesive [5,14–32]. Single and double lap joint tests, where the load is transferred axially across adherends, are frequently used. This load case differs from the loading which is the focus of this work, albeit it shares the same common problem: a stress concentration in the substrate local to the termination of the adherend.

Shang et al. [12] reviewed methods to improve the strength of adhesive joints with composite adherends. They found that two types of solutions were dominant, and that they focused on producing a better distribution of the concentration of load transfer between the adherends, thus reducing peak stresses [33,34]. These methods are: modifying the adherend geometry, and modifying the adhesive fillet geometry.

Adhesive squeezed out of the joint during manufacture may form a fillet. The presence of a fillet increases the load transfer area at the joint edge; this in turn reduces the stress concentration at the edge and has been shown to give a more uniform shear stress distribution [35–37]. Modifying the adherend geometry is commonly achieved by tapering or rounding of the adherend ends. Tapering the adherend ends gives a gradual reduction in stiffness and has been shown to be effective at reducing the stress concentration at the joint edge: Adams et al. [38] achieved strength increases of 200% utilising an inside taper and an adhesive fillet.

In their review, Shang et al. [12] compared the effectiveness of local geometry techniques against other methods in the literature which aimed to increase joint strength. The work of Adams et al. [38] was the equal best of the considered works, and was achieved with a lower manufacturing difficulty than many of the other techniques which focused on global joint configuration.

Whilst tapering of the adherend and use of an adhesive fillet have been shown to be of benefit, a stress concentration remains present: the critical mode of failure is still a fracture of the composite local to the metal adherend edge [38]. In addition, tapering only aims to increase joint strength by reducing the stress concentration; it does not address the unstable nature of damage propagation. A solution to this problem which provides improved stress distributions, and/or which addresses the unstable nature of failure of such joints, would be highly relevant to the various industrial sectors identified in Section 1.2.

1.4. Outline

In this work we develop a novel concept which utilises a profiled adherend edge to address both the strength and the failure stability of metal to composite adhesive joints. First, the novel profiled adherend concept is proposed. We then present our experimental methods, including a Finite Element model developed to guide the specimen design, before outlining the manufacturing and testing processes followed for the experimental study. The results of the work are then presented and discussed, followed by a summary of the key conclusions we have been able to make.

2. Profiled adherend concept

The techniques for improving joint strength from the literature focus on varying the geometry of the joint through the thickness to achieve a gradual stiffness transition and thus a reduced stress concentration

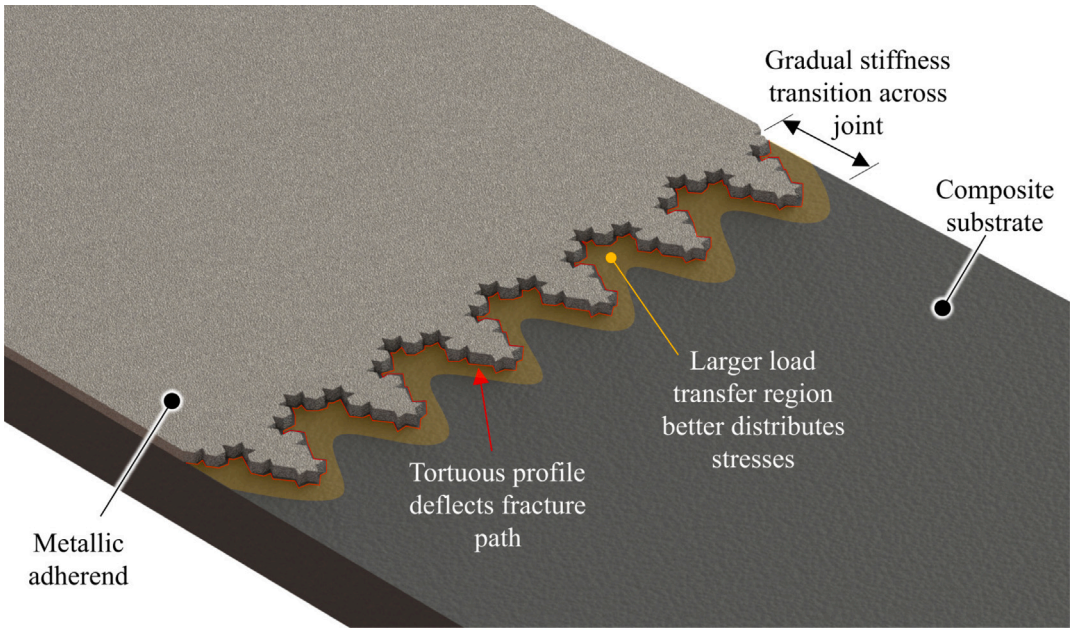

Fig. 2. The proposed concept profiles the adherend edge aiming to improve strength via better distribution of critical stresses and to improve failure stability by deflecting the translaminar fracture path.

at the joint edge. In this work, for the first time in the literature, we vary the profile of the joint edge to achieve these objectives, whilst additionally aiming to address the unstable nature of failure. The concept is depicted in Fig. 2.

The concept aims to reduce the stress concentration in the composite laminate by:

- replacing the discontinuous change in stiffness with a progressive change; and
- increasing the effective length of the joint edge, thus providing a larger region for load transfer;

and to increase the stability of failure by:

- isolating regions of peak stress, making it harder for initiated cracks to propagate; and
- deflecting the path of translaminar fracture, resulting in increased energy dissipation.

In this work, in addition to a straight-edge baseline (Fig. 3(a)), we use a profiled edge based on equilateral triangles (Fig. 3(b)). This triangular profile then serves as an additional baseline when we consider how the parameters of the profile affect performance. We investigate the effect of individually varying: the type of geometry defining the pattern (Fig. 3(c)), the amplitude of the pattern (Fig. 3(d)), the frequency of the pattern (Fig. 3(e)), and the number of length-scales contained within a fractal-based pattern (Fig. 3(f)).

The pointed wave profile, selected to test the effect of the type of profile geometry, is based on an exponential curve; rather than on equilateral triangles, as for the other profile designs.

For the fractal-based pattern, designs of increasing order are displayed in Fig. 4. An example construction of the fractal-based patterns is depicted in Fig. 4(d) for the 3rd order pattern, which we ultimately selected for use as a compromise between the number of length-scales and manufacturing complexity. The fractal-based patterns are constructed by taking sequential Koch curves [39] of increasing order, alternating orientation, and a tripling of size; and then mapping this along the edges of the triangular baseline profile.

3. Specimen design

3.1. Test type and materials

As shown in Fig. 5, a specimen coupon design was chosen which would be loosely representative of key applications of interest, such as an idealisation of a chordwise segment of a jet engine fan blade near the leading edge.

In order to test the merits of the concept, a test was desired which would isolate the failure mode of interest. A quasi-static 4-Point-Bend (4PB) test was selected to apply out-of-plane bending, as opposed to a 3PB configuration, so that the failure location was not prescribed 'a priori'.

The specimen design is depicted in Fig. 6. The adherend edge was positioned at the specimen mid-length. For specimens with profiled adherends, the centre of mass of the profile was consistently positioned at the mid-length. The baseline triangular profile was manufactured with a peak-to-peak amplitude of 5.78 mm and a wavelength of 6.67 mm. These parameters were unchanged for the other profiled designs, with the exceptions that the increased amplitude design had a peak-to-peak amplitude of 17.34 mm, and the increased frequency design had a wavelength of 3.33 mm.

The composite substrate is composed from IM7/8552 pre-preg. The properties of IM7/8552 are given in Table 1. The metallic adherend is grade 5 titanium (Ti_6Al_4V) with the properties shown in Table 2. The adhesive used is AF 163-2K film adhesive by 3M and has the properties displayed in Table 3.

The CFRP layup strategy was selected based on a quasi-isotropic layup, but with the outer 50% of chordwise plies being replaced by spanwise plies, a similar strategy to that which would be anticipated in the industrial applications of interest. The resulting layup was $[(45/90/\text{-}45/90)_2(45/0/\text{-}45/90)_2]_s$, which led to a 4.19 mm thick laminate with a cured ply thickness of 0.131 mm [43].

3.2. Numerical model

We developed a Finite Element (FE) model of the baseline straight edge specimen shown in Fig. 6. The goal of the model was to verify that

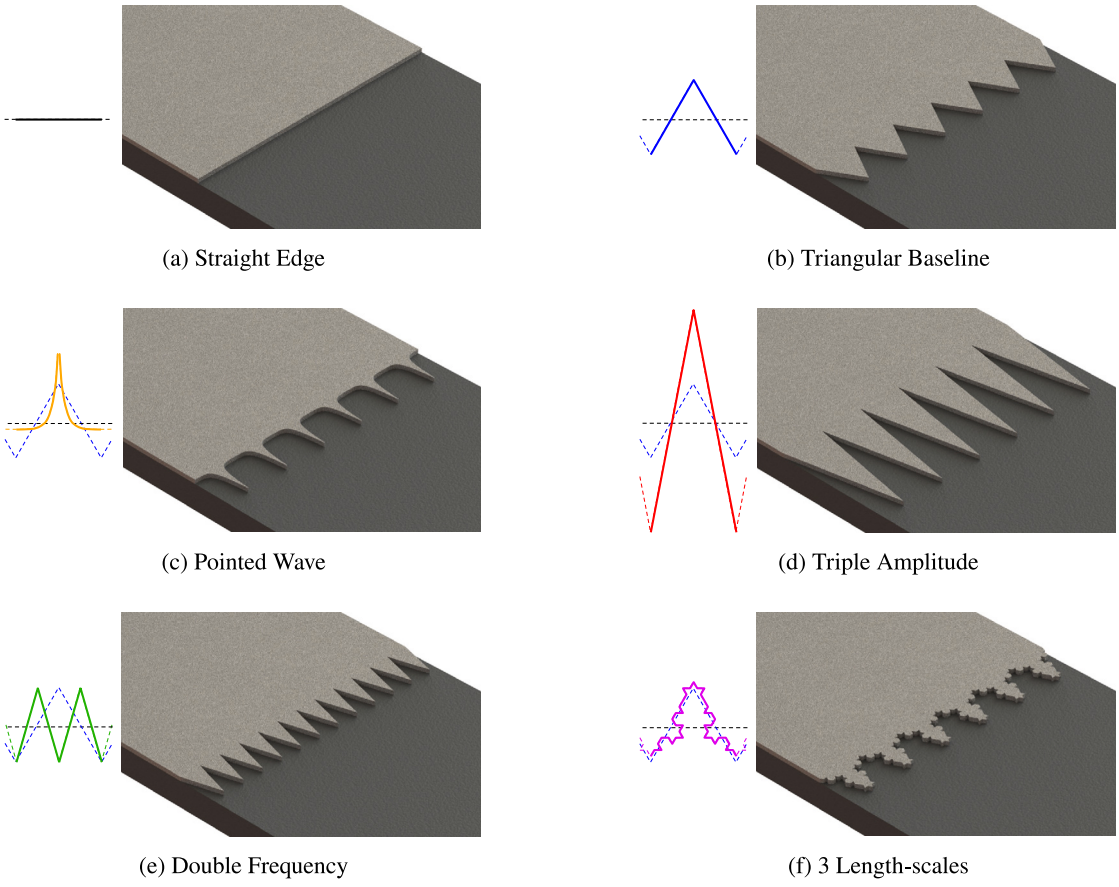

Fig. 3. Repeat units of the various profiles considered alongside renders of each concept.

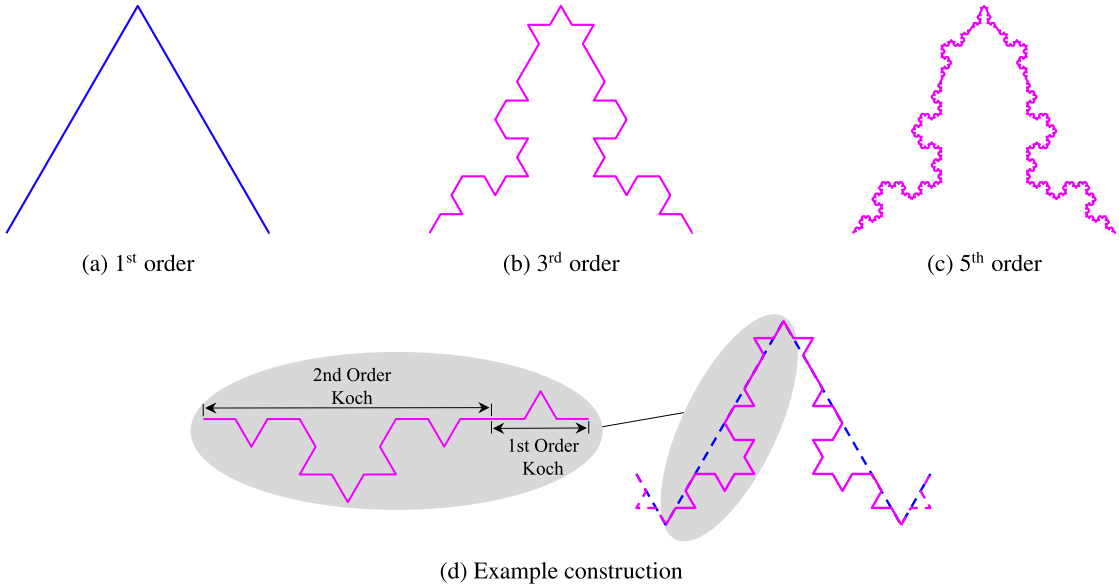

Fig. 4. (a–c) Fractal based patterns of increasing order. (d) Construction of the 3 length-scale fractal-based pattern from Koch curves.

the specimen design would isolate the failure mechanism of interest, by confirming that, for the baseline, the critical failure would be within the composite substrate local to the termination of the metal adherend, and that potentially competing failure mechanisms, such as compressive failure of the laminate or adhesive failure, are not close to being triggered.

The 4PB specimen was modelled using FE in Abaqus standard [53]. The mesh used is shown in Fig. 8. The mesh contains a structured refined region around the joint edge where elements have side lengths equal to the ply thickness of 0.131 mm; a swept region connects this to a structured region with a coarser mesh containing elements with 1 mm side lengths in the plane of the laminate. The six top and bottom plies

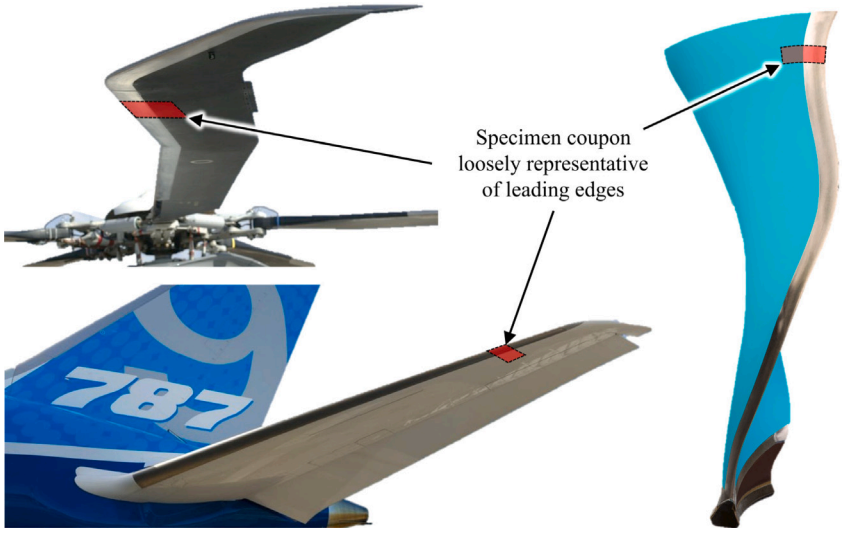

Fig. 5. The test was designed to be loosely representative of a segment of a blade or wing on the leading edge. *Source:* Images from [40–42].

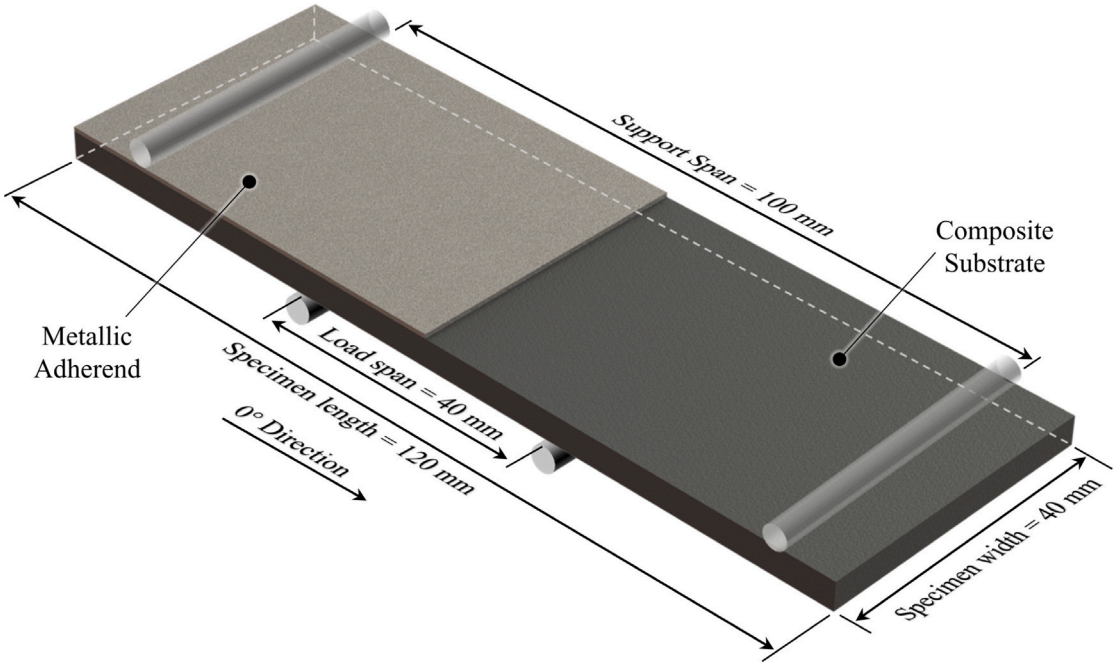

Fig. 6. Specimen design and geometry.

Table 1
IM7/8552 pre-preg material properties.

Elastic properties		Strength properties	
E_{11} (GPa)	161 [44]	Longitudinal Tensile X_T (MPa)	2720 [43]
E_{22} (GPa)	11.4[a]	Longitudinal Compressive X_C (MPa)	1690 [43]
E_{33} (GPa)	11.4[a]	Transverse Tensile Y_T (MPa)	64 [43]
ν_{12}	0.31 [44]	Transverse Compressive Y_C (MPa)	255 [45]
ν_{13}	0.31[a]	Longitudinal Shear S_L (MPa)	101 [45]
ν_{23}	0.435 [46,47]	Transverse Shear S_T (MPa)	101 [45]
G_{12} (GPa)	5.17 [46,47]	Fracture plane angle for pure compression α_0 (°)	53 [48]
G_{13} (GPa)	5.17[a]	Initial misalignment angle ϕ_0 (°)	2.606[b]
G_{23} (GPa)	3.98[a]	Longitudinal shear friction coefficient η_L	0.082 [49]
		Transverse shear friction coefficient η_T	0.287[c]

[a]Assume transverse isotropy.
[b]Validated against longitudinal compressive strength in a single element model.
[c]Calculated [48].

Table 2
Titanium Grade 5 (Ti_6Al_4V) properties.

Properties	
t (mm)	0.635
E (GPa)	111 [50]
ν	0.34 [50]

Table 3
AF163-2K film adhesive properties.

Properties		Plasticity [51]	
		True stress (MPa)	Plastic strain
E (MPa)	1103 [52]	30.10	0.00000
ν	0.34 [52]	41.20	0.00245
Normal Tensile Strength (MPa)	46.93 [51]	46.80	0.00843
Shear Strength (MPa)	46.86 [51]	49.28	0.01637
t (mm)	0.2		

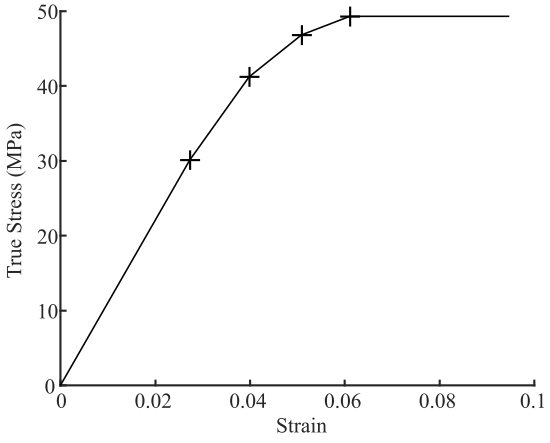

Fig. 7. Stress–strain curve used to define the plasticity of the adhesive. Material data from Santos et al. [51].

are modelled with one element each in the thickness direction, whilst plies far from the surface are grouped in single elements through the thickness direction. Appendix details the convergence study to verify the mesh, and a bending analysis to verify the ply grouping strategy.

The metal and the individually-meshed composite plies are modelled using continuum solid shell elements, whilst the grouped plies are modelled using continuum shell elements with reduced integration. The adhesive is modelled using linear 3D solid elements with full integration.

The composite is modelled as a linear elastic material with damage initiation criterion following the LaRC05 Abaqus subroutine [48,54,55]. The metal is also modelled as a linear elastic material, whilst the adhesive is modelled as an elastic–plastic material with plasticity as defined in Table 3 and Fig. 7.

Boundary conditions have been applied to the model to simulate the set-up shown in Fig. 6. The model is loaded under displacement control at the shown loading locations, whilst zero vertical displacement is enforced at the depicted support locations. Additional boundary conditions are used only to prevent rigid body modes.

3.3. FE model results

Fig. 9 shows the various LaRC05 damage initiation criterion near the joint edge at the onset of failure. It is seen that matrix cracking is critical in one of the plies in tension near the joint edge, whilst the plies under compression have relatively low failure indices. This indicates that failure should initiate significantly earlier local to the adherend edge in the tensile-side composite plies than it would in the compressive-side plies.

Fig. 10 shows the relevant stresses in the adhesive near the adhesive–laminate interface when laminate failure first occurs: these stresses remain below the yield strengths of the adhesive in Table 3. As then expected, the FE model additionally shows that no plastic strain is present in the adhesive. Therefore, the FE model indicates that the adhesive is still operating in the elastic regime at the onset of tensile failure in the composite substrate.

The FE model is therefore successful in the goal of verifying that the specimen design will yield the failure initiation mechanism of interest, and that competing failure mechanisms of compressive composite failure or adhesive failure are not close to being triggered in the baseline specimen, providing scope to observe potentially significant performance improvements when the proposed profiled adherend concept is applied.

4. Manufacturing

The CFRP laminate was manufactured using a hand lay-up process, with the use of alignment pins to ensure accurate ply orientations, and cured as per the manufacturer's recommended cure cycle [43]. Following curing, we verified using a C-scan that the laminates were free of significant defects.

The profiled edges of the metal adherend were manufactured via wire electrical discharge machining. The baseline triangular profile was manufactured with an amplitude of 2.89 mm and a wavelength of 6.67 mm. To achieve sufficient resolution of the pattern, the fractal-based profile was wire eroded using wire with a diameter of 0.1 mm, whilst all other patterns were manufactured using wire with a diameter of 0.25 mm.

We surface-treated the composite substrate and titanium adherend to improve the adhesive bond quality. The CFRP was dry grit-blasted, followed by wiping with degreaser and clean paper towels. As trapped moisture has been shown to reduce the toughness of formed joints [56–58], the laminates were dried at 100°C in a fan-oven for 24 h before bonding.

The surface treatment regarded as the benchmark for titanium alloys is sodium hydroxide anodising [59]. Whilst it is complex and hazardous to apply, it gives long-term durability of joints [60,61]. In this work, we followed the same procedure as used by Feito et al. [59].

When preparing the panels for bonding, we first removed the protective film from one side of the adhesive before placing it against the CFRP substrate and holding it under a vacuum to consolidate. We then removed the protective film from the top surface, before positioning the metal adherends on top via the use of alignment pins, and then we consolidated this under a vacuum.

During curing, we placed a layer of silicone over the exposed adhesive to provide a smooth surface finish. The bond was cured in an autoclave as per the manufacturer's instructions [52]. We placed the adhesive over the entire surface, not just below the adherend, as can be seen in Fig. 11. This allowed a fillet to form naturally from the adherend surface by surface adhesion. The resulting fillets were considered a characteristic of their respective profile.

Six plates like the one shown in Fig. 11 were manufactured, each produced one specimen of each profile type, giving six specimens in total for each configuration. An advantage of this is that any variability in the quality of manufacturing for a single panel would affect just one specimen for each profile type, rather than all specimens of one type.

Following bonding, the specimens were cut from the plates using a water-jet cutter; the initial piercing was performed in the CFRP-only region away from the bonded metal adherend, as piercing in the bonded region can lead to delamination damage. Each test specimen

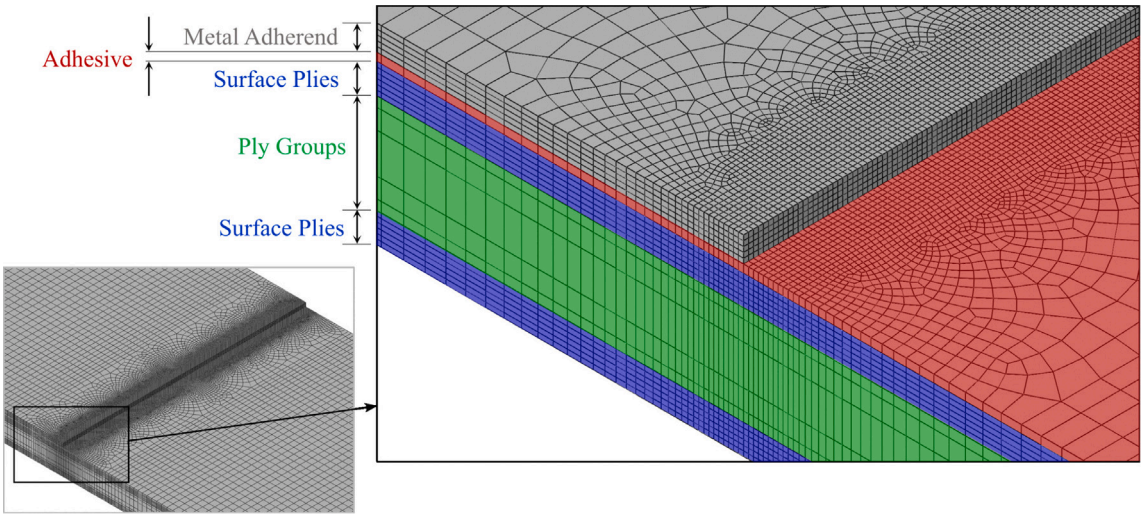

Fig. 8. Detail of mesh refinement around the joint edge. The ply grouping strategy is also visible: the six plies closest to each surface are modelled individually with one element through the thickness, whilst the remaining internal plies are grouped through the thickness to reduce the computational cost of the model.

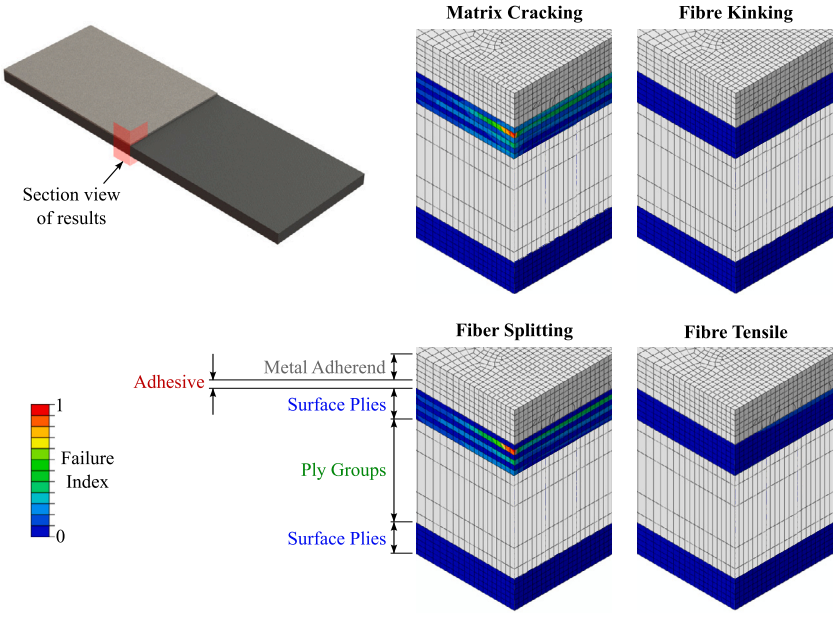

Fig. 9. The different laminate LaRC05 damage initiation criterion at failure initiation. The view is an isometric view of a section cut across the width along the edge of the joint. The matrix cracking failure index reaches a critical value at the specimen edge.

was sanded to 600 grit along the sides to reduce the effect of edge defects.

5. Experimental testing

The 4PB tests were carried out with an Instron loading machine with a 50 kN load cell at a displacement rate of 1 mm/min; the setup is shown in Fig. 12. To ensure all pins made contact at the same time, we raised the support pin on the specimen side without the metal adherend using spacers cut from the same metal plate. We used in-situ acoustic emission monitoring (Express-8 multichannel AE system manufactured by Physical Acoustics) during the tests to provide additional data on the failure process. We used broadband (WD) sensors with an operating frequency range of 100–1000 kHz and the signals were pre-amplified with a pre-amplification level of 20 dB. Two sensors were used during each test, one positioned at either end, with Sonagel W1 used as the coupling agent, and masking tape used to secure them in place. We also recorded video footage during the tests of the specimen edges and, via an inclined mirror, footage of the surface with the bond edge.

6. Results

Fig. 13 exhibits loading curves for representative specimens of each design. The peak load is used as a quantitative measure of the joint strength, but we additionally desired a quantitative Measure of Failure Stability (MFS) of each specimen. For this, we first define the mechanical energy dissipated by the specimen U_m as:

$$U_m = \int_{\delta=0}^{\delta_{uf}} F \, d\delta \tag{1}$$

where F is the force, δ is the displacement, and δ_{uf} is the displacement when unstable failure occurs. Then, we defined the MFS as the energy dissipated prior to unstable failure normalised by the mechanical

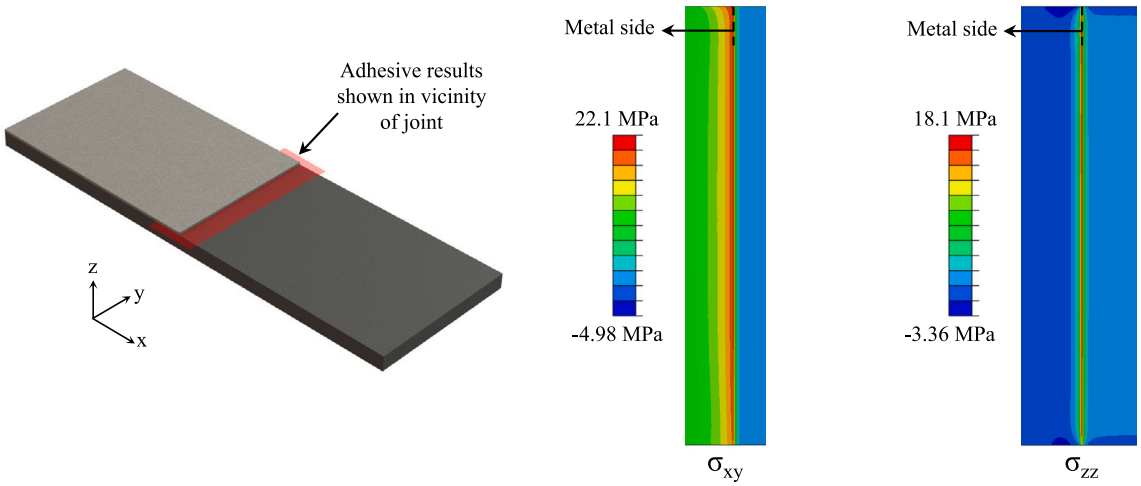

Fig. 10. Contour plots for the adhesive at the joint edge near the adhesive–laminate interface.

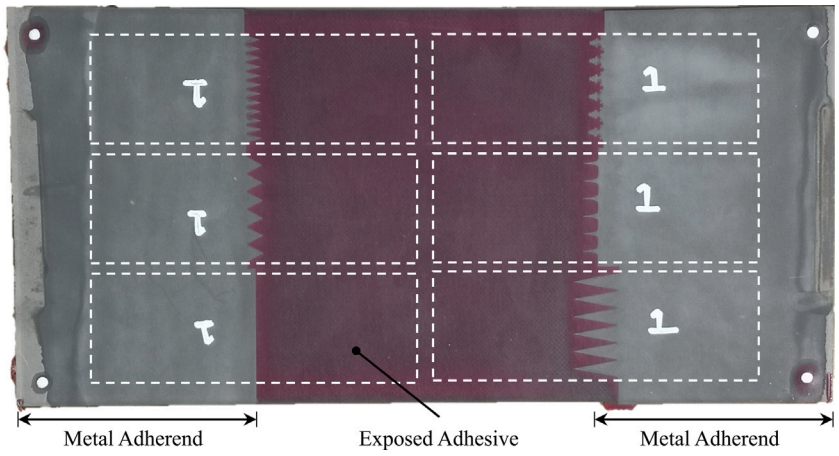

Fig. 11. Each cured panel produced one specimen for each profile type.

energy:

$$MFS = \frac{U_m - 0.5F_{uf}\delta_{uf}}{U_m} \quad (2)$$

where F_{uf} is the force at the onset of unstable failure. This methodology is shown graphically in Fig. 14. The quantitative results for each specimen are plotted in Fig. 15.

Fig. 16 shows p-values, calculated via a two-sample t-test, which compare the quantitative results for each set of specimens against the straight edge and triangular baseline specimen sets. This statistical analysis shows that the quantitative improvements are statistically significant ($p < 0.05$) for the triangular baseline when compared against the straight edge baseline; and that each of the triple amplitude, double frequency, and three length-scale concepts give statistically significant improvements in comparison to the triangular baseline. The quantitative results of the pointed wave profile compared to the triangular baseline profile are seen not to be statistically significant. Fig. 17 displays, for each specimen, the AE events recorded throughout the test; the marker size is scaled logarithmically to represent the energy of each AE event. A universal energy threshold was applied to remove relatively low energy events which occurred from the beginning of each test, leaving AE events associated with damage. Testing images at critical points for a straight edged specimen and a triple amplitude profile specimen are shown in Figs. 18 and 19 respectively. Representative fracture surfaces from a variety of specimens are shown in Fig. 20.

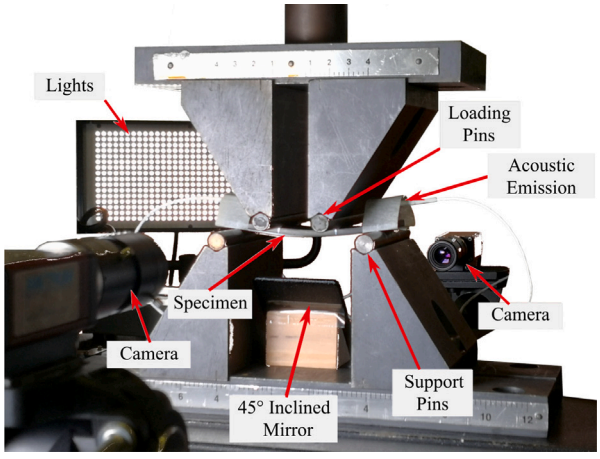

Fig. 12. Experimental 4PB test set up.
Source: Adapted from [62].

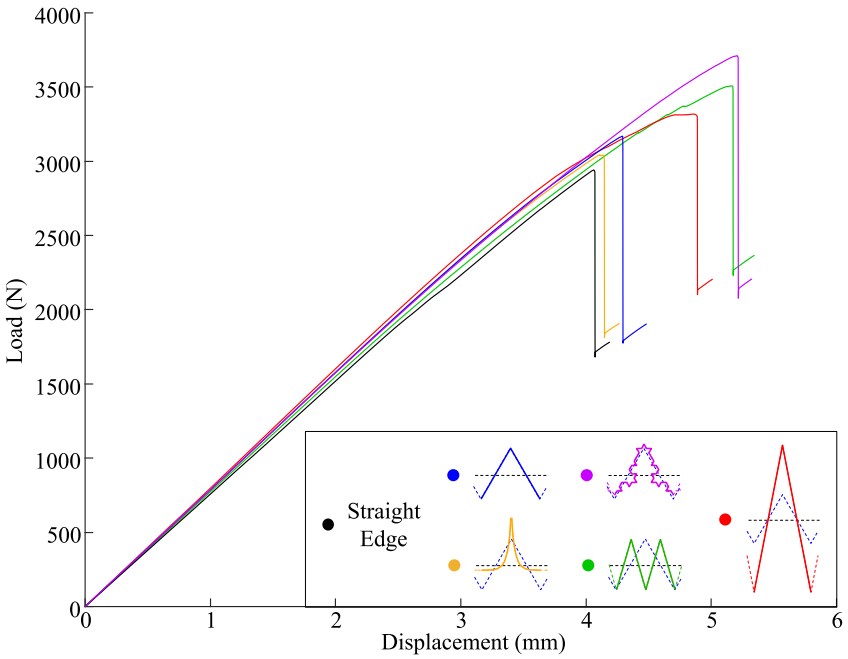

Fig. 13. Loading traces of one representative specimen from each profile design.

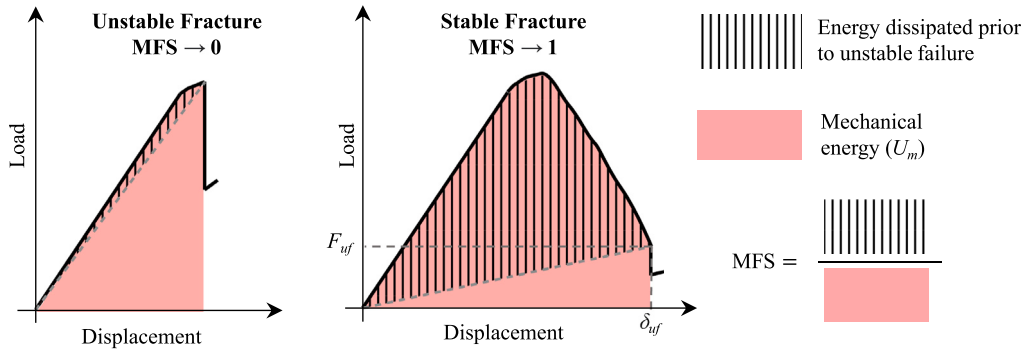

Fig. 14. A schematic to illustrate how we defined a quantitative Measure of the Failure Stability (MFS). The MFS was defined as the energy dissipated prior to unstable failure normalised by the mechanical energy. A fully unstable failure would tend towards a value of 0, where as a fully stable fracture would tend towards a value of 1.

7. Discussion

7.1. Failure mechanisms for the straight edge configuration

The baseline specimens with straight edged adherends exhibited failure initiation in the composite local to the adherend edge as anticipated by the FE model. Immediately before failure, Fig. 18 shows delaminations beginning to originate from an initial matrix crack in the transverse ply. Subsequently, an unstable failure occurs including rapid delamination growth.

The fracture surface seen in Fig. 20(a) reveals that a translaminar fracture has propagated through the specimen, local to the adherend edge. This is the failure mechanism which is of interest, so the sequence of failure in the baseline specimens validates the test and specimen design for investigating our concept (which is designed to address this phenomenon).

7.2. Comparative mechanical performance of profiled adherends

The results shown in Figs. 13, 15 and 16 demonstrate that the profiled specimens exhibit significant increases in mechanical performance relative to the straight edged specimens. The largest improvements in the current work demonstrate that a profiled adherend can result in an increase in the peak load of at least 27%, as achieved with the three length-scale fractal concept. The failure stability of the joint can also be significantly improved, with the profiled specimens in the current work exhibiting regions of stable failure prior to unstable fracture. The improvement in failure stability can be seen quantitatively with the triple amplitude profile concept giving a mean MFS of 0.130 in comparison to 0.035 for the straight edged design.

Fig. 17 shows that, in general, profiled specimens recorded initial AE events at a higher load and displacement than specimens with a straight edged adherend. This suggests that the concept of a profiled adherend is successful in providing better stress distributions and lowering peak stresses, such that initiation of damage is delayed.

The proposal for a profiled adherend edge theorised that a more stable failure would be achieved via deflection of the translaminar fracture. The fracture surfaces shown in Fig. 20 indicate that the profiled adherends were successful in deflecting the translaminar fracture. As seen in Fig. 15, this coincided with an increase in the stability of fracture. However, deflection of the translaminar fracture is not the only toughening mechanism observed. In the profiled specimens, particularly for the triple amplitude specimens, which gave the largest MFS improvement, the fracture surfaces in Fig. 20 show an apparent failure at the metal–adhesive interface around the tips of the profile. Fig. 19 shows the sequence of failure for a triple amplitude specimen.

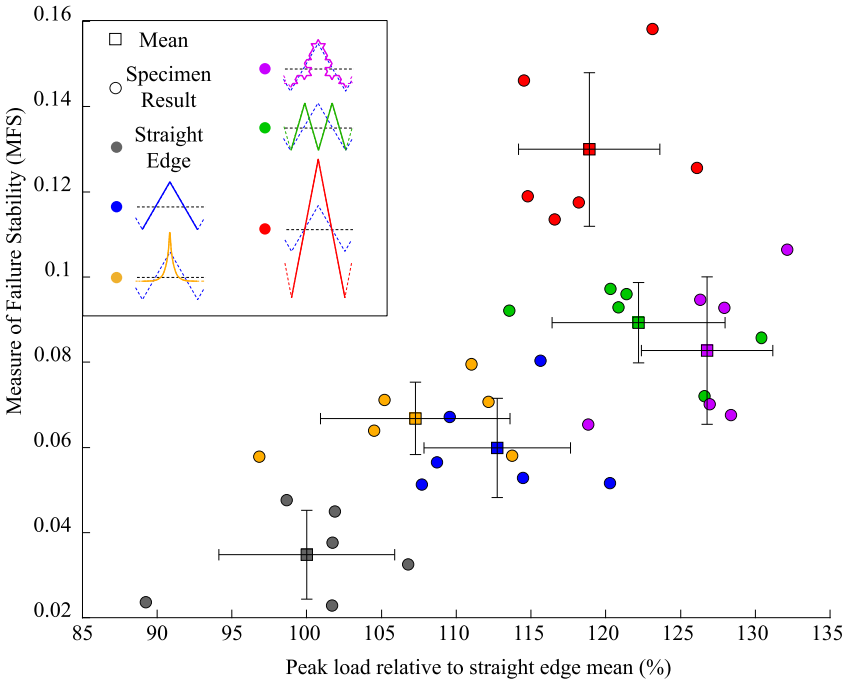

Fig. 15. Peak load against the Measure of Failure Stability (MFS) for all specimens.

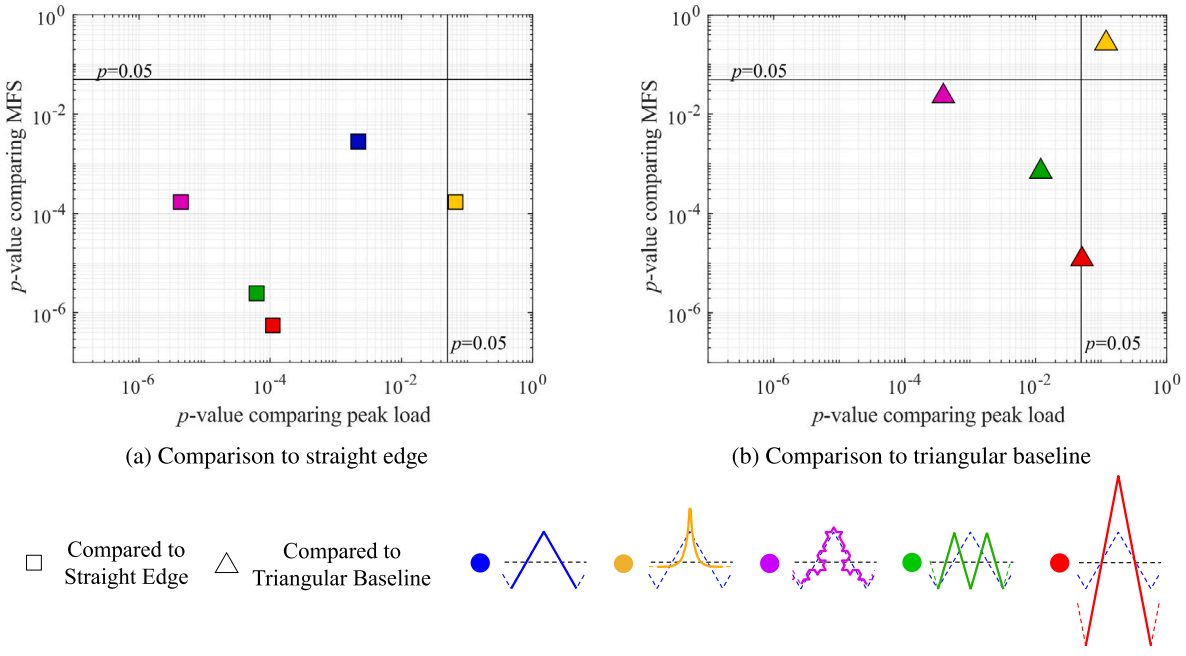

Fig. 16. Statistical significance of the improvement in properties measured.

It can be seen that, before ultimate failure, the profile tips debond and pull away from the surface. A possible explanation for this is that the sharper angle of the triple amplitude profile tip increases the local stress in the adhesive. This triggers some initial adhesive failure before the translaminar fracture, which improves the failure stability, however this is potentially at the expense of even larger increases in joint strength: from the AE results, damage initiation occurs later in the triple amplitude specimens than in the fractal specimens; but the duration of AE events before failure is shorter, and a lower peak load is achieved.

There appears to be scope to produce joints which are significantly more damage tolerant by exploiting this adhesive failure mechanism. If features can be included at the profile tips, which do not significantly affect the stress distribution before failure, but which create a much larger area for debonding, this could allow for significant bridging of the fracture without sacrifices to the increase in joint strength. Avenues to achieve this which could be explored in future work include: using a combination of both profiling and tapering of the adherend edge, or by including weakly attached features at the profile tips.

A valuable piece of future work would be a detailed numerical model verified against these experimental results. This could then be utilised to better understand how changes to the profile change the failure mechanisms, and consequently such a model could be used to create optimised profiles for a range of loading scenarios.

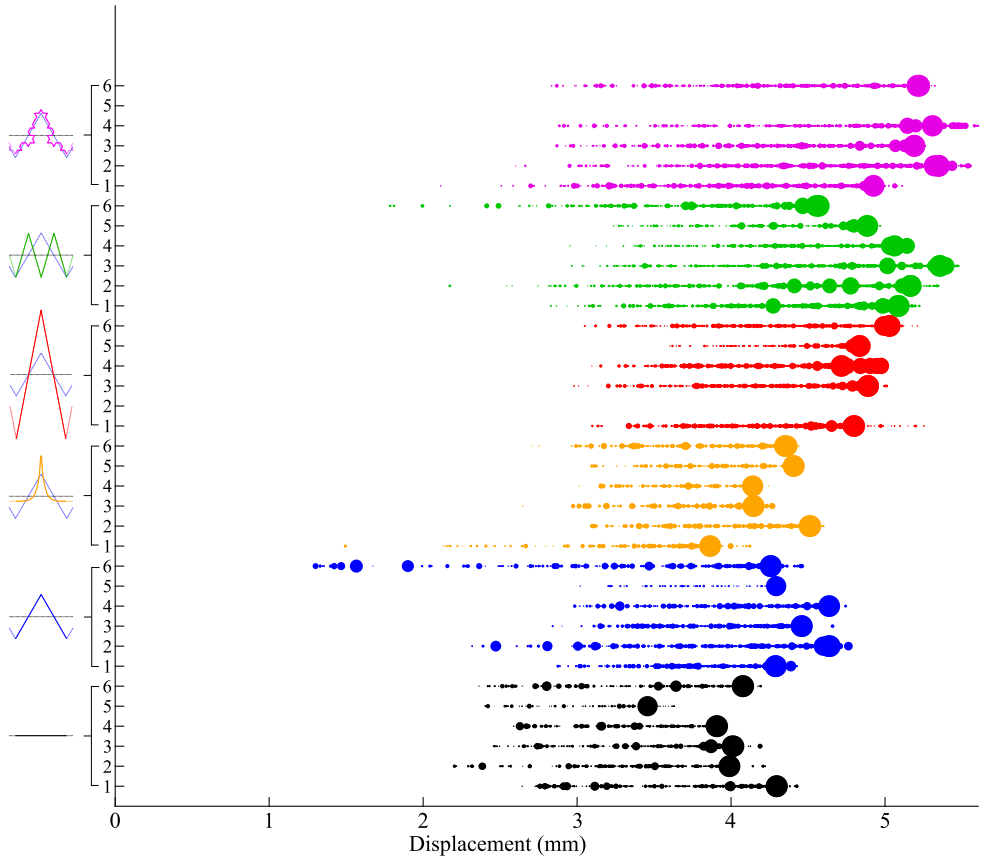

Fig. 17. AE events for each specimen. Markers represent a single AE event with the marker size representing the energy of the event scaled logarithmically.

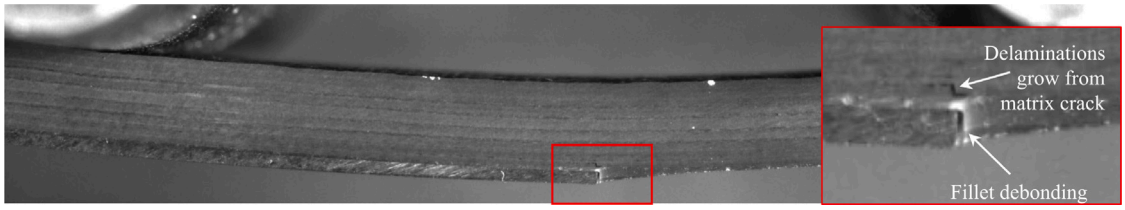

Fig. 18. A specimen with a straight edged adherend immediately before the sudden load drop. Delaminations can be seen to grow from a matrix crack and debonding of the adhesive fillet from the adherend edge is visible.

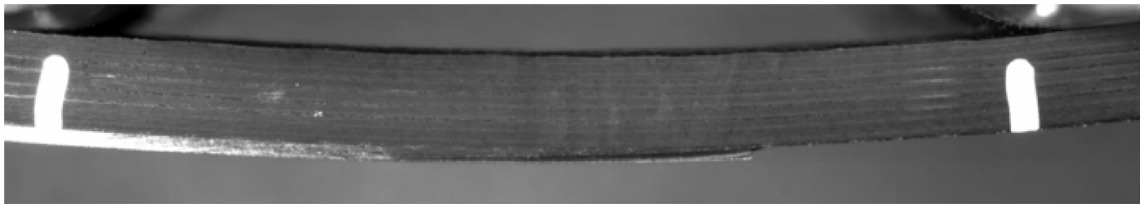

(a) Linear elastic region

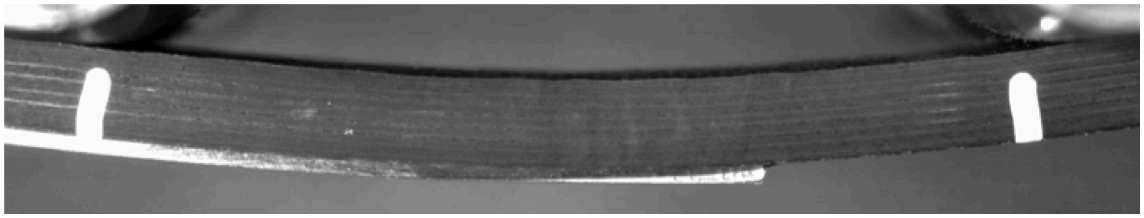

(b) Immediately before sudden load drop

Fig. 19. Side view of a specimen with the triple amplitude profile during testing. The tips of the profile are seen to pull away from the composite before the unstable failure.

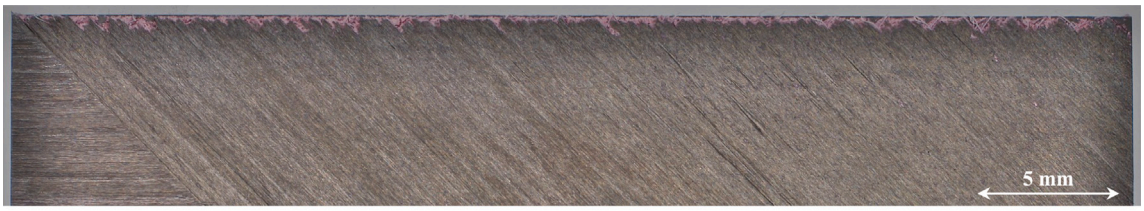

(a) Straight Edge

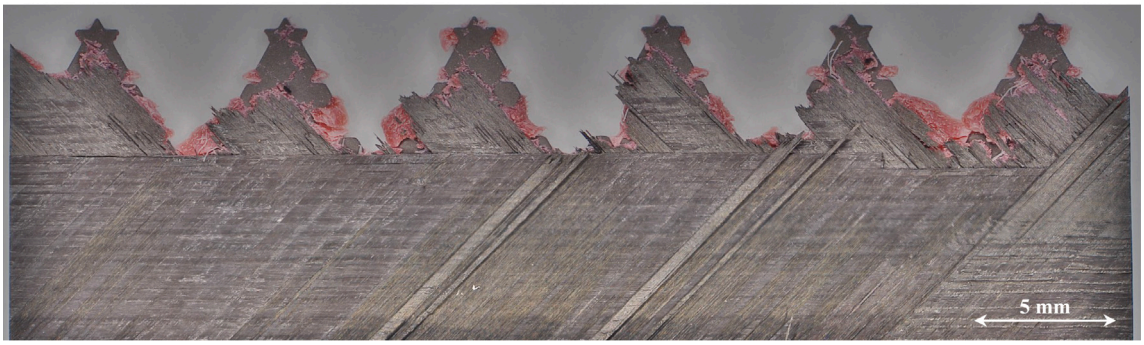

(b) 3 Length-Scale Fractal

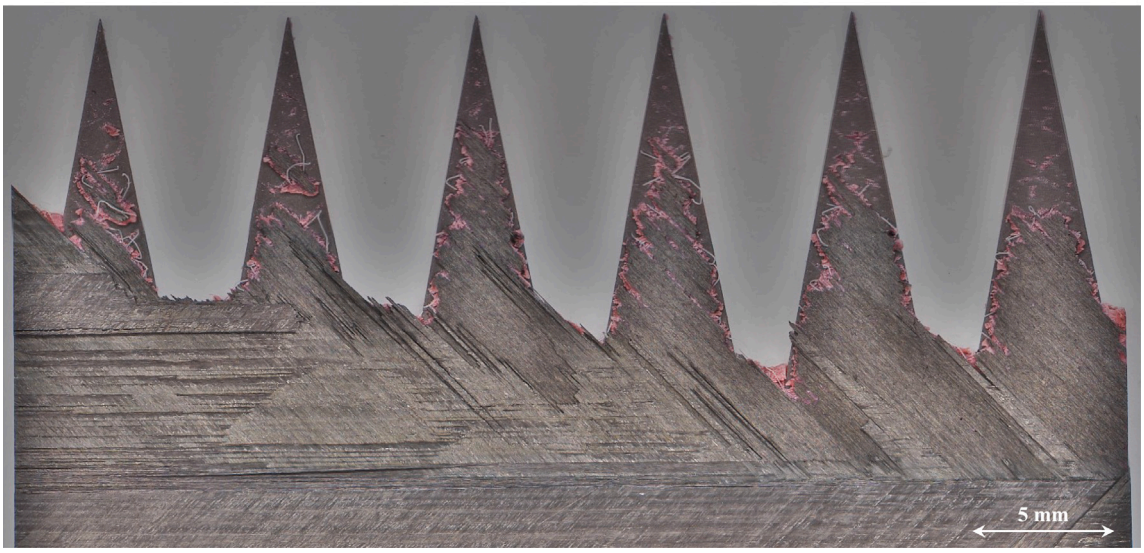

(c) Triple Amplitude

Fig. 20. Representative fracture surfaces on the underside of the metal adherend.

7.3. The effect of varying profile parameters

7.3.1. Alternative style geometry: triangular vs. exponential

The pointed wave profile, based on an exponential curve, was used to compare the effect of the 'style' of geometry chosen for the profile. When compared directly to the triangular baseline concept, the performance of the pointed wave profile design can be seen to be very similar, and statistically there is no significant difference in either metric as per the *p*-values in Fig. 16(b). These results suggest that, for profiled adhesive joints, changes to the 'style' of profile, whilst keeping other variables such as the amplitude and frequency constant, are unlikely to have a significant effect on the mechanical performance.

7.3.2. Triangular profiles with varied parameters

Whilst the presence of the triangular baseline profile yielded significantly improved results relative to the baseline straight edge design, significant further improvements were achieved by varying different parameters of the profile at the adherend edge. In the current work, statistically significant improvements in the mechanical performance were demonstrated, as shown in Figs. 15 and 16, by individually increasing: the amplitude of the profile; the frequency of the profile; and the number of fractal length-scales within the profile.

Whilst each of these changes resulted in improvements to both the peak load and to the MFS, the changes were not linearly proportional across the three modified triangular concepts. The three length-scale fractal profile exhibited the best performance measured by peak load; however, of the three modified profiles, it gave the lowest improvement in the MFS. In contrast, the triple amplitude profile gave the best improvement for failure stability, but of the three modified profiles it gave the lowest improvement in peak load. This suggests that an optimised profile would include increases to profile amplitude and

profile complexity, based upon the relative importance of optimising for each of peak load and failure stability.

In industrial applications where the physical design spaces are much larger than in the current work, such as at the edge of a leading edge erosion shield for a jet engine fan blade or for an off-shore wind turbine, these would allow for much larger increases in profile amplitude, which in turn would allow for more significant increases in profile complexity for a given manufacturing process. The results in the current work demonstrate that significant improvements in mechanical performance are attainable via the use of a profiled adherend edge, and that further significant improvements are attainable by increasing these profile parameters, which supports that this concept has the potential for significant industrial impact. Future work which applies this concept with a much larger profile amplitude and complexity on larger scale tests would be of particular significance to explore the full potential of this concept.

In industrial applications, a decision for the engineer would be the compromise between the benefits of increased mechanical performance of larger and more complex profiles, and the increase in manufacturing time and cost. The balance of this compromise would be very dependent upon the application, as would the manufacturing costs with small applications likely requiring a high precision process, such as wire erosion, to achieve complex profiles, where as larger applications could utilise cheaper manufacturing methods with larger cutting radii, such as water-jet cutting.

8. Conclusions

In this paper we identified the need for a solution to increase the strength, and the failure stability, of metal to composite adhesive joints. We proposed a novel solution to this problem: profiling the termination of the metal adherend, and investigated its effect, focusing on the context of a metallic erosion shield on a composite substrate. Our results demonstrate that by using a suitable profile:

- peak stresses are contained within isolated regions;
- the peak load can increase by at least 27%; and
- the stability of failure is increased.

Our work also shows that this concept can be utilised to obtain further improvements by:

- increasing the profile amplitude (in our tests, tripling the amplitude resulted in a peak load increase of 5.5% and an increase of 117% in the failure stability measure);
- increasing the profile frequency (in our tests, doubling the frequency resulted in a peak load increase of 8.4% and an increase of 49% in the failure stability measure); and
- increasing the number of length-scales (in our tests, incorporating three fractal length-scales into the profile, rather than one, resulted in a peak load increase of 12% and an increase of 38% in the failure stability measure).

In industrial applications where it is feasible to use much larger profile amplitudes, which also allows for larger increases in profile frequency and/or the number of fractal length-scales, we would anticipate that even larger improvements than demonstrated in the current work would be obtainable.

CRediT authorship contribution statement

Adam D. Whitehouse: Conceptualisation, Methodology, Formal analysis, Investigation, Writing – original draft, Visualisation. **Victor Médeau:** Conceptualisation, Methodology, Writing – review & editing, Supervision. **Lorenzo Mencattelli:** Conceptualisation, Methodology, Supervision. **Bamber Blackman:** Investigation, Resources, Supervision. **Silvestre T. Pinho:** Conceptualisation, Methodology, Writing – review & editing, Supervision, Funding acquisition, Project administration.

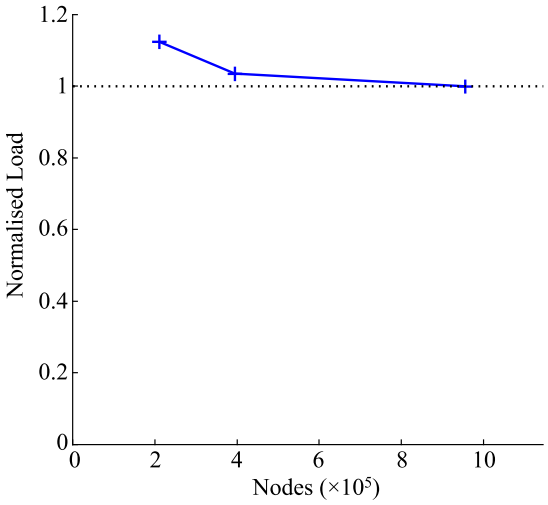

Fig. 21. Mesh convergence study results.

Declaration of competing interest

The authors declare that they have no known competing financial interests or personal relationships that could have appeared to influence the work reported in this paper.

Data availability

Data supporting this study are openly available from Mendeley Data at https://doi.org/10.17632/stg935v3pk.1.

Acknowledgements

The authors would like to gratefully acknowledge the funding for this work from EPSRC, UK DTP 2020–2021 grant reference no. EP/T51780X/1, and the funding from Innovate UK under the UKRI FANDANGO, UK project No. 113232. The authors thank James Finlayson from Rolls-Royce for the helpful discussions on this work. For the purpose of open access, the author has applied a Creative Commons Attribution (CC BY) licence to any Author Accepted Manuscript version arising.

Appendix. FE mesh

A convergence study was conducted to ensure suitable mesh refinement around the edge of the joint. The load when a laminate failure criterion was first reached was compared for three meshes as shown in Fig. 21. The meshes had in-plane side lengths set to half, single, and double the cured ply thickness. It can be seen from Fig. 21 that for a significant increase in computational cost, the change in failure load compared to the most refined mesh was small, in fact just 3.6%, which we considered to be acceptable convergence for the purpose of this model.

To help reduce the computational cost, the plies away from the surface were grouped through the thickness as shown in Fig. 8. The strategy of grouping plies was validated by modelling a laminate in bending and comparing the load when the laminate failure criteria indicated failure, against a model which had an element through the thickness for every ply. The failure load varied by just 0.23% between the two approaches, thus validating this modelling simplification strategy which allowed for models with 40% fewer degrees of freedom, significantly reducing computational cost.

References

[1] Kinloch AJ, Korenberg CF, Tan KT, Watts JF. The durability of structural adhesive joints. London, UK: Applied Science Publication; 1983, URL https://www.researchgate.net/publication/316166213.

[2] Silva LD, Öchsner A, Adams R, editors. Handbook of adhesion technology, first ed.. 2011, URL https://books.google.com/books?hl=en&lr=&id=CsKoeKzXvl8C&oi=fnd&pg=PA1&ots=aSrO5l1vZA&sig=D0F1qhDbvzAMDmuz26uJllxKPm0.

[3] Goland M, Reissner E. The stresses in cemented joints. J Appl Mech 1944;11:A17–27, URL https://www.researchgate.net/publication/237106683_The_Stresses_in_Cemented_Joints.

[4] Hart-Smith L. Adhesive-bonded single-lap joints. (No. NASA-CR-112236). 1973, URL https://citeseerx.ist.psu.edu/viewdoc/download?doi=10.1.1.461.4731&rep=rep1&type=pdf.

[5] Banea MD, M. Da Silva LF. Adhesively bonded joints in composite materials: an overview. J Mater: Design Appl 2009;223(1):1–51. http://dx.doi.org/10.1243/14644207JMDA219.

[6] Kellner T. The art of engineering: The world's largest jet engine shows off composite curves. In: GE News. 2016, URL https://www.ge.com/news/reports/the-art-of-engineering-the-worlds-largest-jet-engine-shows-off-composite-curves.

[7] Rolls-Royce plc. Rolls-Royce starts manufacture of world's largest fan blades – made of composite material – for next-generation UltraFan® demonstrator. 2020, URL https://www.rolls-royce.com/media/press-releases/2020/11-02-2020-intelligentengine-rr-starts-manufacture-of-world-largest-fan-blades.aspx.

[8] Thomas W, Hong SC, Yu CJ, Rosenzweig EL. Enhanced erosion protection for rotor blades. In: Annual Forum Proceedings - AHS International. 3, 2009, p. 2678–86.

[9] Airbus. Composites: Airbus continues to shape the future - commercial aircraft. 2017, URL https://www.airbus.com/newsroom/news/en/2017/08/composites--airbus-continues-to-shape-the-future.html.

[10] Herring R, Dyer K, Martin F, Ward C. The increasing importance of leading edge erosion and a review of existing protection solutions. In: Renewable and Sustainable Energy Reviews. 115, Elsevier Ltd; 2019, http://dx.doi.org/10.1016/j.rser.2019.109382.

[11] Weigel WD. Advanced rotor blade erosion protection system. 1996, Report Number: R–2034. URL https://apps.dtic.mil/sti/citations/ADA314355.

[12] Shang X, Marques EA, Machado JJ, Carbas RJ, Jiang D, da Silva LF. Review on techniques to improve the strength of adhesive joints with composite adherends. Composites B 2019;177:107363. http://dx.doi.org/10.1016/J.COMPOSITESB.2019.107363.

[13] Scarborough C. Technical Journalist Scarbs Tech Ltd, Interviewed by: S. Mansell, Did the Roll Hoop Fail in Zhou's Crash?, YouTube Channel Driver61 6:00-7:25. YouTube; 2022, URL www.youtube.com/watch?v=BpNO1wgUfmY&t=360s.

[14] Adams RD, Harris JA. The influence of local geometry on the strength of adhesive joints. Int J Adhes Adhes 1987;7(2):69–80. http://dx.doi.org/10.1016/0143-7496(87)90092-3.

[15] Fessel G, Broughton JG, Fellows NA, Durodola JF, Hutchinson AR. A numerical and experimental study on reverse-bent joints for composite substrates. In: Collection of Technical Papers - AIAA/ASME/ASCE/AHS/ASC Structures, Structural Dynamics and Materials Conference. 6, American Institute of Aeronautics and Astronautics Inc.; 2007, p. 5829–37. http://dx.doi.org/10.2514/6.2007-2192, URL http://arc.aiaa.org.

[16] Zeng QG, Sun CT. Novel design of a bonded lap joint. AIAA J 2001;39(10):1991–6. http://dx.doi.org/10.2514/2.1191, URL http://arc.aiaa.org.

[17] Chang P, Mouritz AP, Cox BN. Properties and failure mechanisms of pinned composite lap joints in monotonic and cyclic tension. Compos Sci Technol 2006;66(13):2163–76. http://dx.doi.org/10.1016/j.compscitech.2005.11.039.

[18] Kim KS, Yoo JS, Yi YM, Kim CG. Failure mode and strength of uni-directional composite single lap bonded joints with different bonding methods. Compos Struct 2006;72(4):477–85. http://dx.doi.org/10.1016/j.compstruct.2005.01.023.

[19] Liu J, Liu J, Sawa T. Strength and failure of bulky adhesive joints with adhesively-bonded columns. J Adhes Sci Technol 2004;18(14):1613–23. http://dx.doi.org/10.1163/1568561042411295, URL https://www.tandfonline.com/doi/abs/10.1163/1568561042411295.

[20] Reeder JR, Glaessgen EH. Debonding of stitched composite joints under static and fatigue loading. J Reinf Plast Compos 2004;23(3):249–63. http://dx.doi.org/10.1177/0731684404030661.

[21] Beylergil B, Cunedioglu Y, Aktas A. Experimental and numerical analysis of single lap composite joints with inter-adherend fibers. Composites B 2011;42(7):1885–96. http://dx.doi.org/10.1016/j.compositesb.2011.06.010.

[22] Ucsnik S, Scheerer M, Zaremba S, Pahr DH. Experimental investigation of a novel hybrid metal-composite joining technology. Composites A 2010;41(3):369–74. http://dx.doi.org/10.1016/j.compositesa.2009.11.003.

[23] Shang X, Marques EA, Machado JJ, Carbas RJ, Jiang D, da Silva LF. A strategy to reduce delamination of adhesive joints with composite substrates. Proc Instit Mech Eng, Part L: J Mater: Design Appl 2019;233(3):521–30. http://dx.doi.org/10.1177/1464420718805712.

[24] F. M. da Silva L, D. Adams R. Techniques to reduce the peel stresses in adhesive joints with composites. Int J Adhes Adhes 2007;27(3):227–35. http://dx.doi.org/10.1016/j.ijadhadh.2006.04.001.

[25] Budhe S, Banea MD, de Barros S, da Silva LF. An updated review of adhesively bonded joints in composite materials. Int J Adhes Adhes 2017;72:30–42. http://dx.doi.org/10.1016/j.ijadhadh.2016.10.010.

[26] Morgado MA, Carbas RJ, Marques EA, da Silva LF. Reinforcement of CFRP single lap joints using metal laminates. Compos Struct 2019;230:111492. http://dx.doi.org/10.1016/J.COMPSTRUCT.2019.111492.

[27] Akpinar S, Demir K, Gavgali E, Yetim AF. A study on the effects of nanostructure reinforcement on the failure load in adhesively bonded joints after the subjected to fully reversed fatigue load. 98, (13):Taylor & Francis; 2021, p. 1972–97. http://dx.doi.org/10.1080/00218464.2021.1947811, URL https://www.tandfonline.com/doi/abs/10.1080/00218464.2021.1947811.

[28] Demir K, Gavgali E, Yetim AF, Akpinar S. The effects of nanostructure additive on fracture strength in adhesively bonded joints subjected to fully reversed four-point bending fatigue load. Int J Adhes Adhes 2021;110:102943. http://dx.doi.org/10.1016/J.IJADHADH.2021.102943.

[29] Akpinar S. Effects of laminate carbon/epoxy composite patches on the strength of double-strap adhesive joints: Experimental and numerical analysis. Mater Design 2013;51:501–12. http://dx.doi.org/10.1016/J.MATDES.2013.04.037.

[30] Ozel A, Yazici B, Akpinar S, Aydin MD, Temiz S. A study on the strength of adhesively bonded joints with different adherends. Composites B 2014;62:167–74. http://dx.doi.org/10.1016/J.COMPOSITESB.2014.03.001.

[31] Akpinar S, Akpinar IA. Effect of nanostructured reinforcement of adhesive on thermal cycling performance of a single-lap joint with composite adherends. Composites B 2019;175:107106. http://dx.doi.org/10.1016/J.COMPOSITESB.2019.107106.

[32] Akpinar S, Akpinar IA. Influence of carbon and glass fiber reinforced composite adhesive on the strength of adhesively bonded joints. Materials Testing 2023. http://dx.doi.org/10.1515/MT-2022-0284.

[33] Silva LD, Öchsner A. Modeling of adhesively bonded joints. 2008, URL https://link.springer.com/content/pdf/10.1007/978-3-540-79056-3.pdf.

[34] da Silva LF, Campilho RD. Design of adhesively-bonded composite joints. In: Fatigue and Fracture of Adhesively-Bonded Composite Joints. Woodhead Publishing; 2015, p. 43–71. http://dx.doi.org/10.1016/B978-0-85709-806-1.00002-1.

[35] da Silva L, Marques E, Campilho R. Design rules and methods to improve joint strength. In: Silva LFMd, Öchsner A, Adams RD, editors. Handbook of Adhesion Technology. second ed.. Springer International Publishing; 2018, p. 773–810. http://dx.doi.org/10.1007/978-3-319-55411-2{_}27/FIGURES/27, URL https://link.springer.com/referenceworkentry/10.1007/978-3-319-55411-2_27.

[36] Akpinar S, Doru MO, Özel A, Aydin MD, Jahanpasand HG. The effect of the spew fillet on an adhesively bonded single-lap joint subjected to bending moment. Composites B 2013;55:55–64. http://dx.doi.org/10.1016/J.COMPOSITESB.2013.05.056.

[37] Doru MO, Özel A, Akpinar S, Aydin MD. Effect of the spew fillet on adhesively bonded single-lap joint subjected to tensile loading: Experimental and 3-D nonlinear stress analysis. 90, (3):Taylor & Francis Group; 2013, p. 195–209. http://dx.doi.org/10.1080/00218464.2013.777900, URL https://www.tandfonline.com/doi/abs/10.1080/00218464.2013.777900.

[38] Adams RD, Atkins RW, Harris JA, Kinloch AJ. Stress analysis and failure properties of carbon-fibre-reinforced-plastic/steel double-lap joints. J Adhes 1986;20(1):29–53. http://dx.doi.org/10.1080/00218468608073238.

[39] Koch HV. On a continuous curve without a tangent, obtained by an elementary geometrical construction. (Sur une courbe continue sans tangente obtenue par une construction géométrique élémentnire). Arkiv for Matematik (in French) 1904;681–702.

[40] Rolls-Royce plc. The CTi fan system on the advanced low pressure system engine demonstrator. In: Flickr. 2014, URL https://flic.kr/p/nQWSBS.

[41] Wilhelm S. Powerwash gets the bugs off Boeing's secret 787-9 laminar flow system. 2014, URL https://www.bizjournals.com/seattle/blog/2014/05/powerwash-gets-the-bugs-off-boeings-secret-787-9.html.

[42] Paur J. Eurocopter moves one step closer to 'Whisper Mode'. In: Wired. 2010, URL https://www.wired.com/2010/02/eurocopter-moves-one-step-closer-to-whisper-mode/.

[43] HexPly® 8552 Epoxy matrix (180°C/356°F curing matrix). 2020.

[44] Jiménez MA, Miravete A. Application of the finite-element method to predict the onset of delamination growth. J Compos Mater 2004;38(15):1309–35. http://dx.doi.org/10.1177/0021998304042734.

[45] Psarras S, Pinho ST, Falzon BG. Design of composite stiffener run-outs for damage tolerance. Finite Elem Anal Des 2011;47(8):949–54. http://dx.doi.org/10.1016/j.finel.2011.03.011.

[46] Gan KW, Hallett SR, Wisnom MR. Measurement and modelling of interlaminar shear strength enhancement under moderate through-thickness compression. Composites A 2013;49:18–25. http://dx.doi.org/10.1016/j.compositesa.2013.02.004.

[47] Oõbrien TK, Krueger R. Analysis of ninety degree flexure tests for characterization of composite transverse tensile strength. 2001, URL http://www.sti.nasa.gov.

[48] Pinho S, Darvizeh R, Robinson P, Schuecker C, Camanho P. Material and structural response of polymer-matrix fibre-reinforced composites. J Compos Mater 2012;46(19–20):2313–41. http://dx.doi.org/10.1177/0021998312454478, URL http://journals.sagepub.com/doi/10.1177/0021998312454478.

[49] Hongkarnjanakul N, Bouvet C, Rivallant S. Validation of low velocity impact modelling on different stacking sequences of CFRP laminates and influence of fibre failure. Compos Struct 2013;106:549–59. http://dx.doi.org/10.1016/j.compstruct.2013.07.008, URL http://dx.doi.org/10.1016/j.compstruct.2013.07.008.

[50] Ansys. CES Edupack - Materials Database. 2020.

[51] Santos DG, Carbas RJ, Marques EA, da Silva LF. Reinforcement of CFRP joints with fibre metal laminates and additional adhesive layers. Composites B 2019;165:386–96. http://dx.doi.org/10.1016/j.compositesb.2019.01.096.

[52] 3M Scotch-Weld Structural Adhesive Film AF 163-2 Techincal Datasheet. 2009.

[53] Dassault Systemes. Abaqus Standard. 2019, URL https://www.3ds.com/.

[54] Pinho S, Vyas G, Robinson P. Material and structural response of polymer-matrix fibre-reinforced composites: Part B. J Compos Mater 2013;47(6–7):679–96. http://dx.doi.org/10.1177/0021998313476523, URL http://journals.sagepub.com/doi/10.1177/0021998313476523.

[55] Damage initiation for fiber-reinforced composites - SIMULIA user assistance. 2020, URL https://help.3ds.com/2020/english/dssimulia_established/simacaematrefmap/simamat-c-damageinitfibercomposite.htm?contextscope=all#simamat-c-damage-larc05.

[56] Blackman BRK, Kinloch AJ, Paraschi M. The effect of the substrate material on the value of the adhesive fracture energy, G_c : further considerations. In: 1-J. Materials Science Letters. 20, 2001, p. 265–7, URL https://spiral.imperial.ac.uk/bitstream/10044/1/23770/2/Sipral.pdf.

[57] Paraschi M. A fracture mechanics approach to the failure of adhesive joints. 2002, URL https://ethos.bl.uk/OrderDetails.do?uin=uk.bl.ethos.271440.

[58] Blackman B, Kinloch A, Paraschi M, Teo W. Measuring the mode I adhesive fracture energy, G_IC, of structural adhesive joints: the results of an international round-robin. Int J Adhes Adhes 2003;23(4):293–305. http://dx.doi.org/10.1016/S0143-7496(03)00047-2, URL https://www.sciencedirect.com/science/article/pii/S0143749603000472.

[59] Feito DA. Fracture mechanics of carbon fibre reinforced plastics to Ti-alloy adhesive joints (Ph.D. thesis), Imperial College London; 2012, URL https://core.ac.uk/download/pdf/17294419.pdf.

[60] British Aerospace Aircraft Group Weybridge-Bristol Division. Report No. AL/MAT/3864. 1984.

[61] Mahoon A. Titanium Adherends. In: Kinloch A, editor. Durability of Structural Adhesives. London: Elsevier Science Publishers; 1983, URL https://www.bcin.ca/bcin/detail.app?id=77995.

[62] Whitehouse A, Medeau V, Mencattelli L, Blackman B, Greenhalgh E, Pinho S. A novel profiling concept leading to a significant increase in the mechanical performance of metal to composite joints. In: P. Vassilopoulos A, Michaud V, editors. ECCM20 - the 20th European Conference on Composite Materials - Composites Meet Sustainability (Vol 2). Lausanne, Switzerland: EPFL Lausanne, Composite Construction Laboratory; 2022, p. 708–15. http://dx.doi.org/10.5075/EPFL-298799{_}978-2-9701614-0-0, URL https://infoscience.epfl.ch/record/298799.